Physicochemical investigation of Portland cement pastes prepared and cured with seawater

Yangyang Zhang, Yanjie Sun, Peiliang Shen,

Jianxin Lu, Yamei Cai, Chi Sun Poon *

(Department of Civil and Environmental Engineering, The Hong Kong Polytechnic University, Hung Hom, Kowloon, Hong Kong, China)

*Corresponding author

E-mail: cecspoon@polyu.edu.hk (C.S. Poon)

Abstract

The direct use of both seawater and sea sand in concrete production has been becoming attractive for some marine and coastal engineering where the availabilities of freshwater and river sand are limited. To further expand the use of seawater (e.g., using seawater as both mixing and curing water), this work provided fundamental research regarding the effects of using seawater as the mixing and curing water on the physicochemical properties of Portland cement pastes. The sub-samples at different depths of the seawater mixing and curing samples were extracted and separately analyzed. The chemical changes were quantitatively investigated, and the relation between the physical behaviors and the chemical changes was studied. The results showed that in the outer region of the samples, the ettringite content was significantly increased, but the content of Friedel's salt was slightly reduced. Moreover, a large amount of calcium hydroxide was dissolved, but correspondingly, magnesium hydroxide (MH) crystals with various particle sizes were formed. Also, the sodium ions in the seawater were incorporated into the structure of calcium silicate hydrate gel, resulting in the formation of silica dimers with a shorter silica chain and the increase of nanopore volume (increasing by 22% in the inner region and 36% in the outer region). In addition, seawater increased the ion transport rate, but the blocking effect of the MH crystals on the samples largely decreased the rate. The changes in the crystalline and amorphous hydration products potentially influenced the strength development.

Keywords: Seawater; Quantitative characterization; Chemical evolution; Physical change

1. Introduction

Concrete is the most widely used construction material owing to its characteristically positive attributes, e.g., (i) low cost, (ii) convenient maintenance, (iii) flexible workability, (iv) good strength and durability, (v) excellent resistance to weather and erosion, etc. **[1, 2]**. The amount of

freshwater required for concrete mixing reaches about 1.5 billion tonnes per year **[3, 4]**. As the World Meteorological Organization estimated **[5]**, over 50% population worldwide will have difficulties accessing enough freshwater for daily life by 2050. Thus, the consumption of freshwater for concrete production would further exacerbate the freshwater shortage.

Besides freshwater, the huge consumption of river sand for concrete production also poses a continuing threat to river ecosystems, flood control, and navigation **[3]**. Desalted sea sand, as an alternative to river sand, has been used as the fine aggregate in concrete production in many countries around the world. However, the usage of sea sand in steel-reinforced concrete raises safety and durability problems owing to the immature technology and inadequate monitoring **[3]**.

Seawater sea-sand concrete (SSC), as a novel and potentially sustainable construction material, is receiving increasing interest across the world **[3, 6]**. But the ions in seawater and sea sand would easily cause steel corrosion in steel-reinforced concrete, which poses a great threat to marine and coastal infrastructures **[7, 8]**. Thus, SSC can only be applied in limited applications, including plain concrete, and ordinary structural concrete using corrosion inhibitors for protecting steel; however, with the invention and application of fiber-reinforced polymer (FRP), the replacement of steel reinforcement in concrete with FRP has provided the potential to develop SSC, due to the good corrosion resistance to seawater of FRP **[9-11]**. Research on the SSC structures reinforced with FRP is being actively pursued in several research groups. But most of the work mainly focused on the structural behavior of FRP-SSC and the durability of FRP bars in SSC environments. Regarding plain cement paste, mortar, or concrete using seawater or sea sand, the research findings of their properties are inconsistent, including whether the compressive strength is similar, higher, or lower when compared with the freshwater mixed counterparts **[3, 6, 11-14]**. Generally, most researchers agreed that the compressive strength of seawater or/and sea-sand concrete was increased at an early age, but became slightly lower in the medium and long term compared to the freshwater concrete **[3, 11-13]**.

This work is based on a research project aiming to provide recommendations for the design of SSC structures for marine infrastructure, i.e., fiber-reinforced polymer-seawater sea sand concrete (FRP-SSC), especially for the development of some coastal areas and remote islands where the availabilities of river sand and fresh water are limited. FRP-SSC structures, as a new and environment-friendly structure, are proposed and are of great practical relevance. Also, marine concrete would be exposed to seawater soon after it is cast.

Previous works, focusing on seawater corrosion, found that the main hydration products include ettringite (AFt), calcium hydroxide ($Ca(OH)_2$, CH), C-S-H gel, magnesium silicate hydrate (M-S-H) gel, Friedel's salt, magnesium hydroxide ($Mg(OH)_2$, MH), and $CaCO_3$ **[15-18]**. According to thermodynamic modeling, when hydrated in low levels of seawater, Friedel's salt would be formed instead of monocarboaluminate ($C_4A\hat{C}H_{11}$). But C-S-H and AFt would be decomposed probably due to low pH, and the total volume of the hydrated phases would be reduced in very high levels of seawater, along with the additional formation of M-S-H, hydrotalcite, MH, and $CaCO_3$ **[17]**.

Concerning the seawater mixed Portland cement pastes, it is generally agreed that seawater would accelerate the heat flow and increase the hydration heat. It was reported that about 40% of chloride in seawater would be bound by Friedel's salt **[14]**, but Montanari et al. **[19]** found that the Friedel's salt content was negligible in the seawater OPC paste, at ~0.47 wt.% at 28 d using TG-DTG measurement; and more Cl^- was physically absorbed by C-S-H gel.

For areas where freshwater is scarce, seawater may also be used as curing water. To essentially design high-performance SSC applied in marine structures, this work provides a fundamental understanding of Portland pastes prepared and cured with seawater. Different depth regions in the paste were chosen to quantify the phase evolution. The changes in hydration products were quantitatively characterized, and the long-term products were simulated by thermodynamic modeling. The relation between physical behaviors and chemical changes was studied.

2. Experimental procedure

2.1. Materials

A commercially sourced OPC (CEM 52.5) with a specific gravity of 3.15 was used. Fig. S1 shows the different physicochemical properties of this OPC. X-ray fluorescence (XRF) measurement of OPC was done using a Supermin200 instrument (Rangaku Corporation, Japan). The Rietveld refinement result (Fig. S1 (b)) shows that the mineral composition of OPC was composed of 66.4 wt.% of C_3S, 11.9 wt.% of C_2S, 6.0 wt.% of C_3A, 7.2 wt.% of C_4AF, 2.7 wt.% of $C\check{S}H_2$ (gypsum) and 5.8 wt.% of $CaCO_3$. The ICSD database used in this work was shown in Table S1. Fig. S1 (c) shows the particle size distribution of OPC determined by using a Malvern MS3000 laser particle analyzer, and the mean particle size was 16.95 um. The NMR result (Fig. S1 (d)) shows there was only one Si-O signal (Q0) present in the OPC, corresponding to the presence of C_3S and C_2S.

A C_3S produced from a laboratory was also used. It had a 90.7 wt. % purity tested by XRD and calculated by Rietveld refinement, and the other materials were 8.9 wt% C_2S and 0.4 wt% CaO.

Glenium SP8S, polycarboxylate-based superplasticizers produced by BASF Co. Ltd, was used in this work with a specific gravity of 1.05. The compositions of the artificial seawater, prepared according to ASTM D1141-98 (2013), are shown in Table S2.

2.2. Specimen preparation

To evaluate the influence of using seawater as mixing and curing water on the physicochemical properties of OPC pastes, two OPC pastes were prepared: mixed and cured with either seawater

(SS sample) or deionized (DI) water (DD sample as the reference sample). OPC paste cubes with a W/C ratio of 0.38 were prepared for microstructure analysis. OPC powder was mixed with DI water or seawater for 1 minute at a low speed and mixed for 1 minute at a high speed. Then the OPC pastes were cast in 40 mm × 40 mm × 40 mm cubes, vibrated for 30 seconds by an electromagnetic vibration generator system, covered by a plastic wrap, and placed in the laboratory at 23 ± 2 °C for 1 day. Afterward, the specimens were demoulded and cured in DI water or seawater at 23 ± 2 °C until test ages. For each curing age, three 2 mm thick slices from the samples (i.e., the outer region (0 mm - 2 mm), the middle region (10 mm - 12 mm), and the inner region (20 mm - 22 mm)) were cut by a diamond saw. The samples used for microstructure tests were taken from the middle zone of each cut slice, were subsequently ground, immersed in isopropanol to avoid further hydration, and then dried in a vacuum desiccator [20].

To more accurately determine the composition of the C-S-H gel formed in DI water and seawater, a simplification by analyzing the C-S-H gel formed by the hydration of a synthesized C_3S was used since (i) C_3S is the dominant mineral and it controls the early hydration of OPC, and (ii) the C-S-H formed by the OPC pastes in this study would be inevitably intermixed with other complex hydration products and largely influence the FE-SEM/EDS analysis. The C_3S was mixed with DI water and seawater separately using a W/C ratio of 10 to easily separate the C-S-H gel from other hydration products. After the initial mixing, the hydrated samples were sealed in a PE bottle and cured for 28 days at 23 ± 2 °C. Then the solids were obtained using a 0.45 μm membrane filter paper, immersed in isopropanol, and then dried in a vacuum desiccator.

To evaluate the macro-performances of the cement pastes prepared with different strength grades, the specimens were prepared with two water-to-cement (W/C) ratios (viz. 0.28 (0.5% Superplasticizer (SP8S) was added) and 0.38 (no superplasticizer)). The preparation and curing procedures were the same as those mentioned above. At each curing age, three cubes of each batch of the specimen were removed and tested for compressive strength using a loading rate of 0.96 kN/s.

2.3. Microstructure characterizations

Electrochemical impedance spectroscopy (EIS) was performed by a Multi-AutolabM 204 instrument with a frequency of 1 Hz to 1 MHz and an AC signal magnitude of 10 mV. A two-electrode system was used in this work. The impedance spectra were analyzed using Nova 1.11 software.

X-ray diffraction (XRD) data were obtained by a Rigaku Smartlab high-resolution X-ray diffractometer, operating with a tube voltage of 45 kV and a tube current of 200 mA. The whole data acquisition time was 30 minutes at 5.0°-80.0° 2θ with a 0.020° step size, ensuring a good signal-to-noise ratio. The mineral and hydration product compositions were quantified by Rietveld refinement using TOPAS 5.0 software. 10 wt% α-Al_2O_3 (Aladdin, 99.99% purity), as an internal standard, was well mixed with the samples to calculate the crystalline and noncrystalline (Acn) phases. The global refined parameters were set, including background coefficients, phase scale factors, zero-shift error, Chebyshev polynomial correction, Lorentz polarization factor, cell parameters, and crystal structures. Table S1 shows the ICSD codes used for quantitative analysis.

Thermogravimetric curves (TG) were recorded by a Rigaku Thermo Plus EVO2 instrument. The heating procedure was from 30°C to 1000°C with a heating rate of 10°C/min. ~10 mg hydrated powder was placed in an open corundum crucible and tested under an N_2 atmosphere.

The Mercury intrusion porosimeter (MIP) test was done by a Micromeritics AutoPore IV 9500 Series instrument with a maximum mercury intrusion pressure of 207 MPa. The slices cut from the specimens were broken into small fragments manually, and particles with dimensions of ~5 mm were chosen, soaked in isopropanol, and dried in a vacuum desiccator before the MIP analysis.

Field-emission scanning electron microscopy (FE-SEM) observations were performed by a Tescan MAIA3 with an accelerating voltage of 5 kV. Energy dispersive spectroscopy (EDS) measurements were also carried out with an accelerating voltage of 20 kV.

^{29}Si magic angle spinning nuclear magnetic resonance (^{29}Si MAS-NMR) measurements were carried out by a GEOL 500 MHz spectrometer equipped with a probe of 7-mm CP/MAS, a rotation rate of 4500 Hz, and a resonance frequency of 79.5 MHz. The ^{29}Si MAS-NMR spectra per sample were recorded using a relaxation delay of 30 seconds and the scans of over 2000.

Nitrogen adsorption and desorption measurements were done by an ASAP 2020 Micromeritics Accelerated Surface Area and Porosimetry instrument. The bath temperature was −196 °C. The sample powders were firstly preheated at 60 °C for 24 hours. The pore size distribution was

obtained by Barrett-Joyner-Halenda (BJH) analysis.

Gibbs free energy minimization software (GEMS) was used to simulate the evolution process of the equilibrium phases for the seawater mixed and cured cement paste. During this calculation process, the PSI-Nagra database [21] and Cemdata 18 database [22] were used. This seawater mixed and cured cement paste was simulated in the modeling through the progressive addition of seawater to the seawater mixed cement paste. The quantity of seawater in this calculation varied from 0 to 32,000 mL per 100 g of anhydrous cement. It assumed that the surface of the seawater mixed cement paste was in contact with an infinite amount of seawater, and the inner part of the paste was exposed to a very low amount of external seawater.

3. Results

3.1 Quantitative change of crystalline hydration products

Firstly, the compositions of crystalline products in different regions of DD and SS pastes changed significantly, as shown in Fig. 1 and Fig. S2. During the hydration of the DD sample at 1 day, CH crystals and AFt crystals were detected, along with the four unreacted clinkers. For OPC mixed with seawater, Friedel's salt was formed in the SS sample at 1 day. This crystalline phase had also been widely reported by others [14, 16, 23]. The compositions of crystalline products in the specimens cured in DI water or seawater differed noticeably. Regarding the DD sample, hemicarboaluminate, a new crystalline product, was formed after 7 days of hydration. However, the ettringite (AFt) peak decreased after 7 days and was hardly detected at 28 days. For the SS sample, the XRD peak of AFt formed in the outer region increased after 7 days, and was significantly higher at 28 days, indicating that using seawater as the curing water significantly

affected the chemical properties of the exposed surface of the SS sample. Previous studies using seawater as the mixing water but not seawater curing only reported the formation of AFt but did not observe the evolution process [14, 24]. In this work, for the SS samples, the content of AFt obviously increased in the outer region due to the presence of SO_4^{2-} ion in the curing seawater. However, the trend for Friedel's salt was dramatically different as the content of Friedel's salt did not show an increase in the outer region although seawater contained a large amount of Cl^- ion.

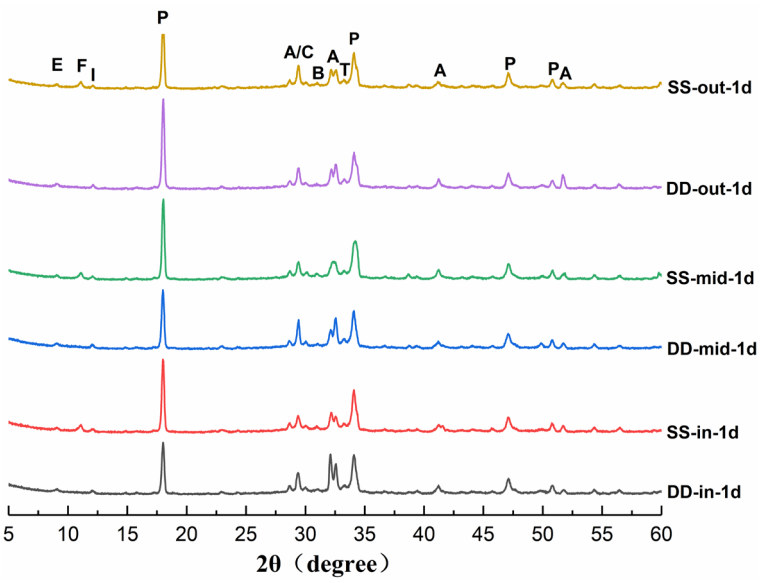

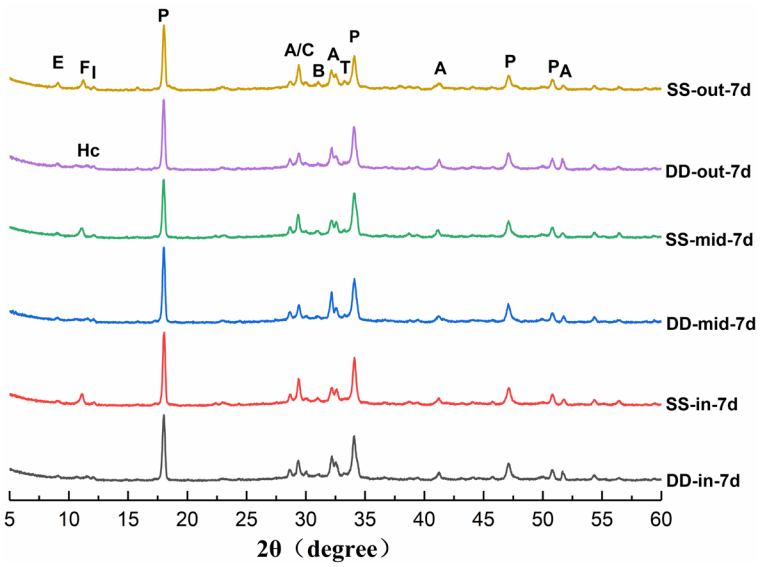

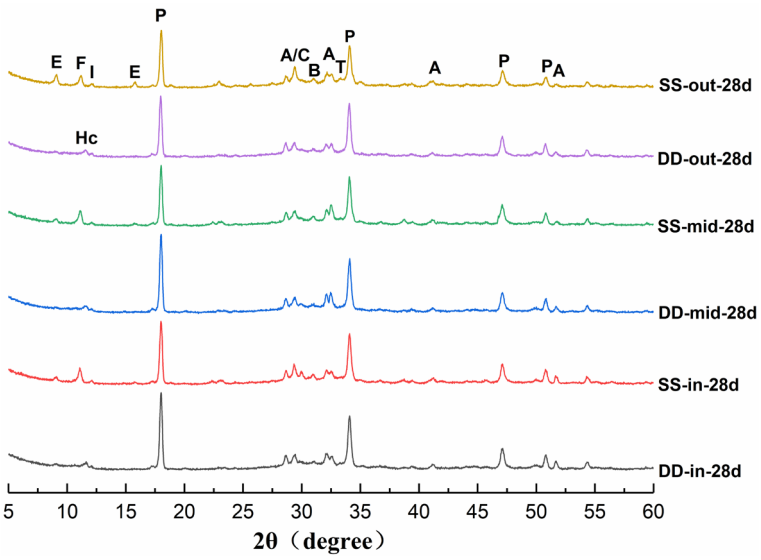

Fig. 1 XRD patterns of DD and SS pastes at 1, 7 and 28 days. (Legend: E: ettringite (AFt); F: Friedel's salt; Hc: hemicarboaluminate; P: CH; A: C_3S; B: C_2S; T: C_3A; I: C_4AF; C: Calcite)

Secondly, the changes in crystalline hydration products and unhydrated clinker minerals were further quantitatively characterized, as shown in Table 1. The Rietveld plots for the outer region of the SS sample at 28 days, as a quintessential example, as shown in Fig. S3. C_3S, as the main early-hydration mineral, was quantified to assess the influence of seawater on the hydration degree (Table 1 and Fig. S4). The hydration degree of C_3S increased in all regions of DD and SS samples as the curing age increased. In addition, the hydration degrees of C_3S in all the regions of the SS sample at all hydration ages were higher compared to the DD sample, which directly confirmed the acceleration effect of seawater. But the acceleration effect was slight at a later age.

The changes in CH content in DD and SS samples were different, as shown in Table 1. Owing to the accelerated effect of seawater, a larger amount of CH was formed in all the regions of SS pastes compared to the DD pastes at 1 day. But after subjecting to DI or seawater curing for 7 days,

the CH content of the SS samples, especially in the outer region, was lower than that in the DD sample. The changes in mass loss of CH in the TG-DTG results (Fig. S2) also confirmed the quantitative XRD results. In addition, as shown in Table 1, the 1-day AFt contents were similar for the DD and SS pastes, and the AFt contents were also similar in the inner and middle regions of the two pastes at 7 days. But there were obvious differences in AFt contents in the outer regions of the two pastes after the specimens were cured in DI water and seawater respectively. In addition, this difference became more obvious at 28 days as the AFt in the DD sample was transformed into hemicarboaluminate. However, AFt in the SS sample was present in all regions. For Friedel's salt, it was only formed in the SS sample, but its content in the outer region was slightly lower compared to the other two regions. Thus, for the later-age samples prepared with seawater curing, sulphate attack would contribute to the formation of gypsum formed by the reaction of CH and sulphate ions, and then the formed gypsum reacted with aluminate phase to form AFt, along with a decrease of Friedel's salt [25]. This phenomenon was more evident on the surface of samples where the seawater attack was more serious.

Table 1 Quantitative XRD results by the Rietveld method (with an error of measurement ±2%) in different regions of DD and SS samples at 1, 7, and 28 days. (%)

Sample	C_3S	C_2S	C_3A	C_4AF	Calcite	CH	AFt	Friedel's salt	Acn[a]	Rwp[b]
DD-in-1d	21.7	12.0	2.9	8.1	6.5	14.3	1.8	-	32.7	11.9
SS-in-1d	18.8	13.7	3.8	6.2	8.7	15.0	1.5	3.8	28.4	12.9
DD-mid-1d	22.5	13.8	4.3	7.3	6.4	13.7	1.5	-	30.6	12.7
SS-mid-1d	18.8	11.6	2.7	6.6	8.9	15.2	1.4	5.1	29.5	11.1
DD-out-1d	21.8	12.6	3.1	6.9	6.2	13.0	1.9	-	34.5	11.1
SS-out-1d	20.2	13.4	2.6	6.7	9.8	14.8	1.6	5.4	25.7	10.3
DD-in-7d	17.9	13.4	1.7	5.1	7.2	20.1	1.1	-	33.5	13.4
SS-in-7d	17.3	9.3	2.0	3.5	7.7	19.3	1.1	6.2	33.5	12.6
DD-mid-7d	17.0	11.9	2.0	7.0	6.5	20.5	1.1	-	29.7	13.4
SS-mid-7d	15.2	10.6	2.1	4.4	8.3	18.9	0.9	7.0	32.7	11.0
DD-out-7d	14.9	12.7	2.0	5.1	7.5	21.8	1.4	-	34.7	12.4
SS-out-7d	13.0	11.0	1.8	6.5	8.5	14.9	3.4	6.2	34.6	11.7
DD-in-28d	10.7	10.2	1.4	3.0	5.4	20.9	-	-	48.3	12.8
SS-in-28d	9.7	9.3	1.3	2.2	6.6	16.7	1.3	7.0	46.0	12.3
DD-mid-28d	10.3	10.9	0.6	3.3	5.7	20.6	-	-	48.6	13.3
SS-mid-28d	9.7	10.8	0.7	3.1	6.3	16.0	1.6	6.5	45.3	12.6
DD-out-28d	10.3	9.3	0.9	2.7	6.1	22.6	-	-	48.2	12.7
SS-out-28d	9.3	9.9	0.5	2.5	8.5	14.4	5.4	5.7	43.8	11.4

-: not present.

[a]: amorphous and non-quantified crystalline phase

[b]: weighted-profile R value

3.2 Change of C-S-H gel

Fig. 2 shows the ^{29}Si MAS-NMR spectra of two hydrated pastes at 28 days. The deconvoluted data were obtained using Gauss's formula and the geometric area method by the Peakfit 4.12 software. Table 2 shows the Si distribution, polymerization degree, mean molecular chain length, and fraction of vacant tetrahedral sites of C-S-H gel. Generally, the ^{29}Si MAS-NMR spectra of OPC pastes might have five signals of Q^n structural units, i.e., Q^0, Q^1, Q^2, Q^3, and Q^4 [26-28]. No Q^3 or Q^4 signals were detected in Fig. 2, confirming that the amorphous SiO_2 gel was not present.

The structure of C-S-H gel in DD and SS samples differed substantially. Table 2 shows that the polymerization degree and mean molecular chain length of C-S-H gel in the SS sample were smaller than that in the DD sample, but an opposite trend was found in the fraction of vacant tetrahedral sites. Thus, the polymerization degree and mean molecular chain length of C-S-H gel obviously decreased, and the vacant tetrahedral sites increased with using seawater as the mixing and curing water.

Nitrogen adsorption and desorption measurements were carried out to analyze the change of nanopores of the C-S-H gel. Fig. 3 shows the BJH adsorption dV/dD pore volume of DD and SS samples at 28 days. Generally, the gel pore between C-S-H particles is below 10 nm [29, 30]. The results showed the pore volume below 10 nm of SS sample was obviously larger compared to DD sample. In addition, the pore volume in the outer region of SS sample was significantly larger compared to the inside region, i.e., the total pore volume of SS-in sample was 0.066 cm^3/g, increasing by 22% compared with the DD-in sample (0.054 cm^3/g), and that of SS-out sample was 0.076 cm^3/g, largely increasing by 36% compared with DD-out sample (0.056 cm^3/g).

Fig. 4 shows that the chemical compositions of C-S-H gel in the two samples were different, i.e., trace amounts of sodium and chloride were found in the structure of C-S-H gel in the seawater hydrated C_3S pastes. Previous works also found that Cl^- ion can be physically absorbed in the structure of C-S-H gel formed in the seawater or present in Cl-containing solutions, and the absorbed Cl^- ion content was about 3-18 mg Cl^-/g C-S-H [19, 31-34]. Regarding alkali cations incorporated in the structure of C-S-H gel, Lothenbach et al. [35], synthesizing C-S-H gel with

different Ca/Si ratios equilibrated in sodium hydroxide solutions, found that sodium would replace calcium, and was present at the surface or in the interlayer space of C-S-H, resulting in a reorganization of C-S-H structure, further reducing the mean molecular chain length of C-S-H gel. This result was also further confirmed in this study, i.e., the mean molecular chain length of the C-S-H gel formed by seawater mixing and curing OPC pastes also decreased due to the uptake of sodium, as shown in Fig. 4 and Table 2.

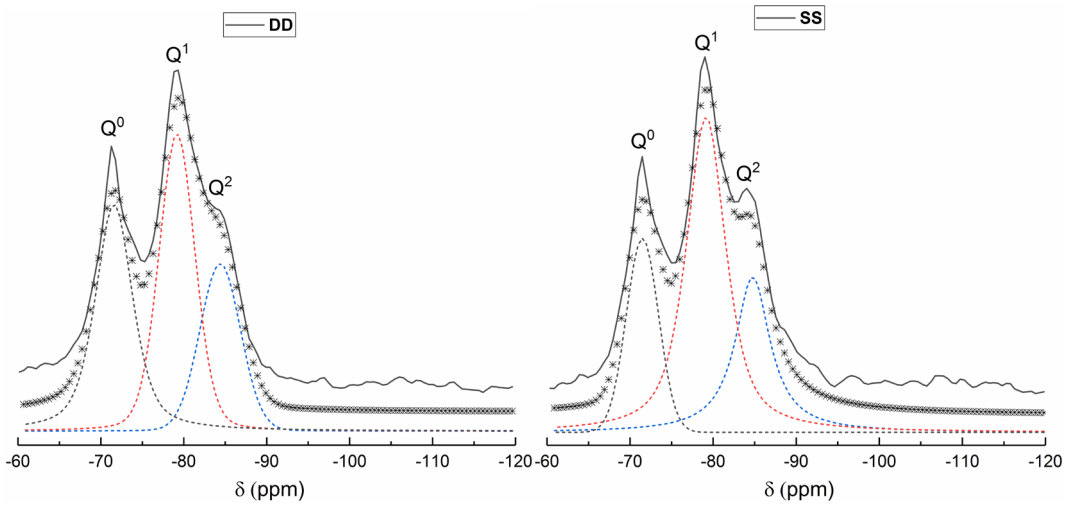

Fig. 2 ^{29}Si MAS-NMR spectra of OPC and different hydrated pastes.

Table 2 Population distribution of Q^0, Q^1, and Q^2 resonances and characterization parameters of deconvoluted ^{29}Si MAS-NMR spectra, with a peak-fitting error ~2%.

Sample	Q^0(%)	Q^1(%)	Q^2(%)	PD[a]	MCL[b]	v[c]
DD	36.30	39.86	23.84	0.598	3.20	0.238
SS	20.20	53.43	26.37	0.493	2.99	0.251

[a] Polymerization degree of C-S-H, PD = Q^2/Q^1. [26]

[b] Mean molecular chain length of C-S-H, MCL=$2(Q^1+Q^2)/Q^1$. [26, 27]

[c] Fraction of vacant tetrahedral sites, v = 1/(MCL+1). [36]

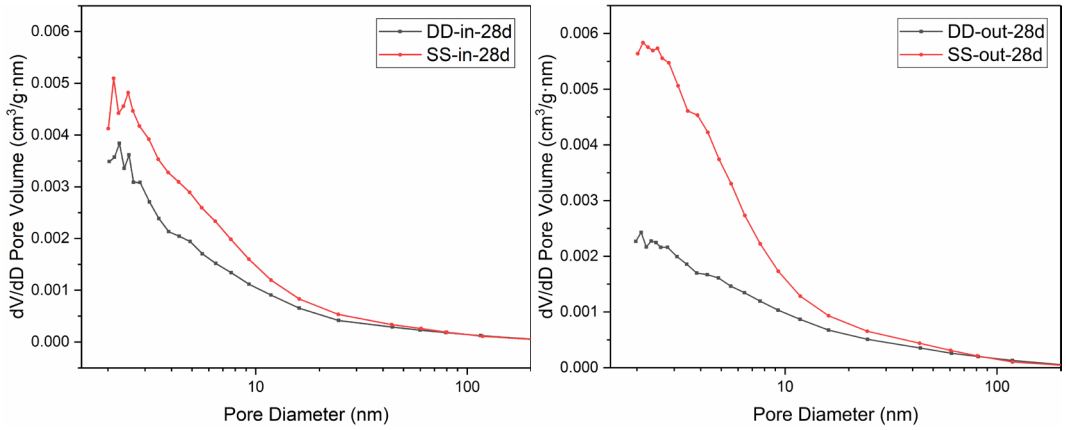

Fig. 3 BJH adsorption dV/dD pore volume of DD and SS samples

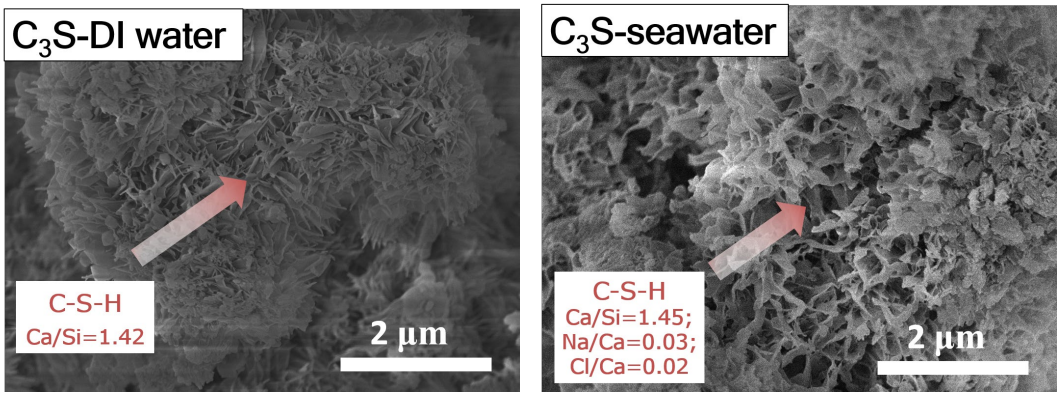

Fig. 4 SEM-EDS data of C-S-H gel in two C_3S pastes with a W/C ratio of 10

3.3 New hydration products

Friedel's salt, a new Cl-containing crystal phase, was formed in the SS sample. This work further determined the amount of Friedel's salt in different regions of the sample. As shown above, the amount of Friedel's salt was similar in the outer, middle, and inner regions.

On the other hand, $Mg(OH)_2$ (MH) crystals with different particle sizes were formed. Firstly, the two cement pastes showed different physical external appearances, as shown in Fig. S5, i.e., the DD sample exhibited the common characteristic appearances. However, a white powder could be

clearly observed on the surface and in the seawater cured SS sample.

The white powder deposited in the solution of the SS sample was collected and analyzed, as shown in Fig. 5. Fig. 5b shows that the white powder was mainly consisted of MH, as well as some calcite, aragonite, and huntite. Previous works also reported the formation of MH on concrete surfaces subjected to seawater corrosion or immersed in Mg-containing solutions [16, 23, 37-39], but few studies adequately characterized the formed MH and compared the differences between the MH formed in the solution and the MH grew on the concrete surface. And the main weight loss was located at about 360°C in the TG-DTG curves (Fig. 5c) corresponding to the dehydration of MH. In addition, bundles of agglomerated MH crystals, proven by SEM-EDS data (Fig. 5f), grew together and formed some large globules, as shown in Fig. 5d. The formed MH crystals exhibited a lamellar morphology with a relatively small particle size of about 500 nm (Fig. 5e).

The white powder found on the surface of the SS sample was also analyzed, as shown in Fig. 6. The XRD result, as shown in Fig. 6b, indicated that MH crystal was the main product of the white powder on the surface of the SS sample, along with some small XRD peaks of calcite. Meanwhile, the mass loss of MH was also detected in the TG-DTG curves (Fig. 6c). The results of SEM and EDS images (Fig. 6d-f) also further confirmed the presence of MH. Compared with the MH crystal found in the solution (Fig. 6e), the MH crystals formed on the surface exhibited a larger particle size, about 2 μm; and the thickness of the MH crystal layer increased significantly, as shown in Fig. 6e, although these MH crystals were also formed with a lamellar morphology. And

the dehydration temperature of this MH was 390°C, which was significantly higher than the MH formed in the solution (at 360°C), and confirmed that the particle size of the MH crystal formed on the surface was larger than that formed in the solution.

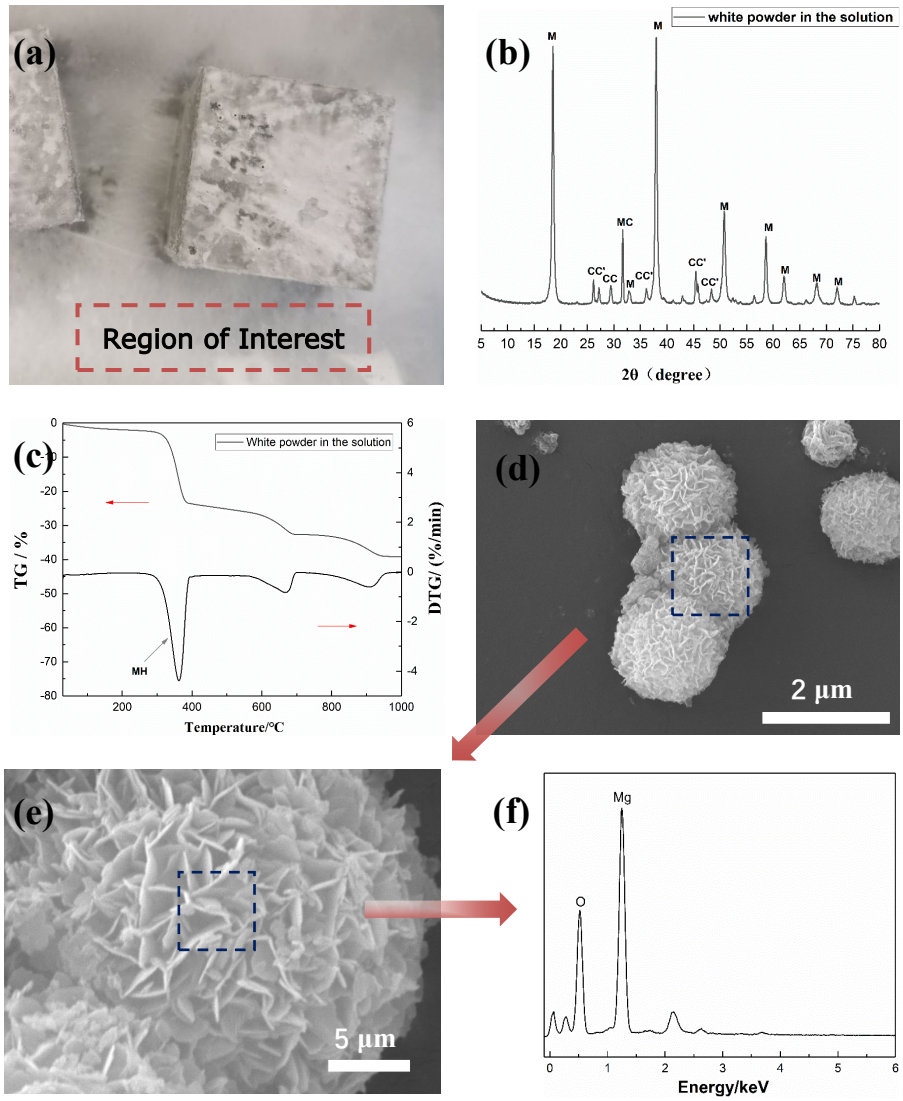

Fig. 5 (a) Region of interest in the SS sample, in which the microstructure tests were carried out; **(b)** XRD pattern of the white powder in the solution, legend: M: $MH(Mg(OH)_2)$; CC: calcite; CC': aragonite; MC: huntite; **(c)** TG-DTG curves of the white powder in the solution; **(d)** SEM image of the white powder in the solution; **(e)** Enlarged region on SEM image; **(f)** EDS image of the white powder in the solution.

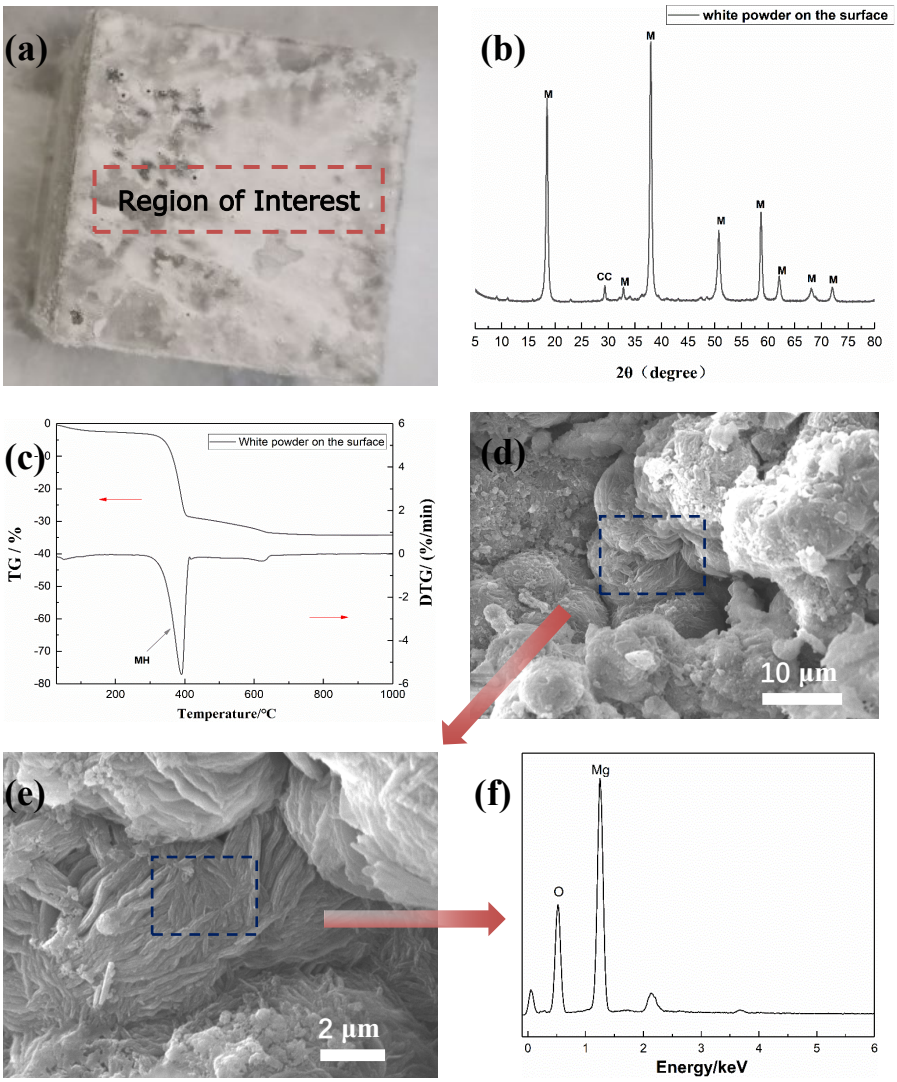

Fig. 6 (a) Region of interest in the SS sample, in which the microstructure tests were carried out; **(b)** XRD pattern of the white powder on the surface, legend: M: MH($Mg(OH)_2$); CC: calcite; **(c)** TG-DTG curves of the white powder on the surface; **(d)** SEM image of the white powder on the surface; **(e)** Enlarged region on SEM image; **(f)** EDS image of the white powder on the surface.

Normally, CH crystals are continuously precipitated, indicating that the pore solution is initially supersaturated with respect to CH, and CH gradually stabilizes at the equilibrium concentration. The pH of the saturated CH solution is around 12.5 [40]. But the pH of the saturated MH solution is around 10.5 [41]. When the SS sample was cured in seawater, the concentration of OH^- ion with

respect to MH in seawater increased dramatically, the ion activity product (K_{s0}) with respect to MH increased correspondingly, and the saturation index (SI) with respect to MH was greater than zero. Thus, Mg^{2+} ions in the seawater rapidly reacted with OH^- ion on the surface of the SS sample, resulting in the formation of MH on the surface or in the solution. For CH, as the pH of the pore solution in the outer section of the SS sample dropped, the OH^- ion, and K_{s0} with respect to CH decreased correspondingly, and thus the pore solution was unsaturated with respect to CH, which rendered the formed CH gradually dissolved to release OH^- ion. Thus, the CH content in the outer region of the SS sample dramatically decreased, as shown in Table 1 and Fig. S2. The excess Ca^{2+} would transfer to (i) the surface to react with CO_3^{2-} and form calcite (Fig. 6b), or (ii) the solution to form metastable aragonite or stable calcite (Fig. 5b). In addition, the slight decrease of pH in the outer section also favored the formation of AFt [34, 42], which was also verified by the XRD result (Fig. 1) and TG-DTG result (Fig. S2).

3.4 Change of physical properties

Fig. 7 shows the compressive strength of DD and SS samples using two W/C ratios at different curing ages. The compressive strength of the SS sample was higher than that of the DD sample at 1 day since the hydration degree of OPC pastes was effectively improved by seawater. However, the compressive strength of the SS sample prepared with both W/C ratios obviously decreased starting from 7 days, compared to the DD sample. Thus, the changes in the outer exposed parts had an obviously negative impact on the compressive strength when the samples were cured in seawater. Moreover, the MIP result at 28 days shows that the porosity (above 10 nm) of the SS

sample was 13.8 % and increased by 5.3% compared with the DD sample.

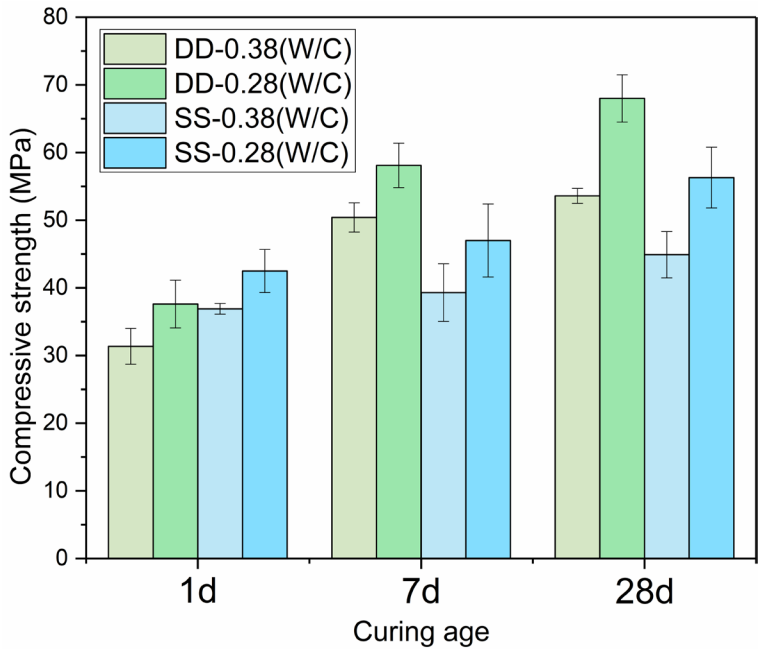

Fig. 7 Compressive strength of seawater OPC pastes

Fig. 8 shows the EIS results of DD and SS samples at 1, 7 and 28 days. Impedance modulus, as an index evaluating the durability of concrete, is denoted by the intersection value between the bulk arc and electrode arc in the x-axis of EIS curves [43]. With an increase in the impedance modulus, the ion transport becomes more difficult, suggesting that external ions are harder to enter the internal zone of the sample. The impedance modulus of DD and SS specimens at each W/C increased with increasing hydration age. And the impedance modulus of both samples improved at all curing ages with the use of a lower W/C ratio. In addition, the SS sample had a lower impedance modulus at 1 day compared to the DD sample. Interestingly, the impedance modulus of the SS sample using the W/C ratio of 0.28 decreased more than that of the W/C 0.38 sample. However, the impedance modulus of the SS sample became higher at 28 days; in addition, the impedance modulus of the SS sample with the W/C ratio of 0.38 was much higher than the DD

sample at 28 days, compared to the results at 7 days.

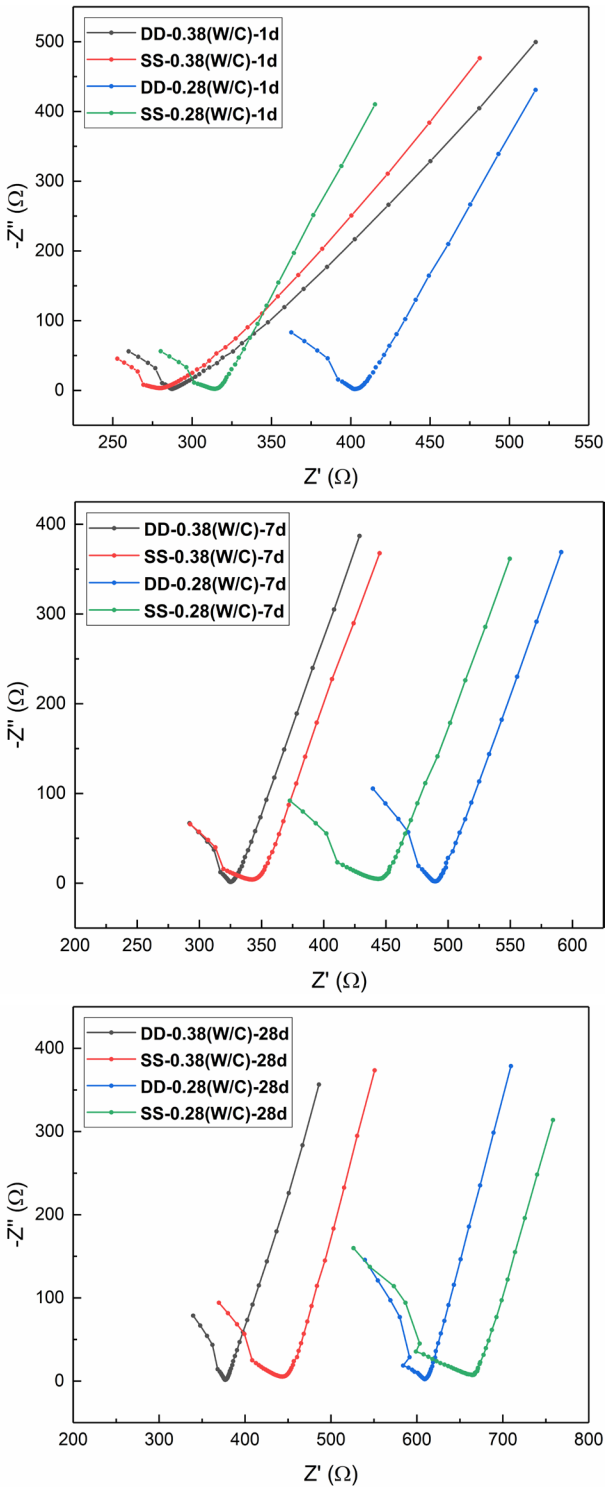

Fig. 8 EIS results of DD and SS samples at different curing ages.

4. Further discussion

4.1 Further influences of seawater used as both mixing and curing water compared with using seawater as mixing water only

The macro-performances and microstructures of Portland specimens using seawater as the mixing water only had been reported in previous works. With respect to the compressive strength, the seawater mixed pastes, mortar, or concrete had high early-age strength and slightly low or similar later-age strength compared to freshwater mixed concrete [3, 6, 11-13]. In this work, a high early-age strength was also found; but an obvious decrease in strength was observed starting from 7 days when the pastes were cured in seawater (Fig. 7).

The ions in seawater can accelerate the hydration rate of Portland cement, making the hardened pastes show a high early-age strength [4, 14, 19]. In Fig. S4, seawater obviously improved the hydration degree at 1 day, by about 5.6%; and this accelerating effect was still obvious at 28 days although it became lower (about 1.3%). Also, the change of CH content was unsuitable for assessing the hydration degree at the later age owing to the dissolution of CH in the SS sample (discussed in Section 3.3), and thus the determination of the hydration degree of C_3S by the Rietveld method was the most direct and accurate method to assess the acceleration effect of seawater on the hydration of cement at the later age.

Comparing the use of seawater as only the mixing water [6, 14, 44] with using seawater as both mixing and curing water, MH, as a new hydration product, was obviously formed with a lamellar morphology on the surface of the paste where its particle size was larger compared to that formed

in the cured seawater. Furthermore, the CH contents in the outer region of the paste were also significantly lower while MH was formed. A larger amount of AFt was also formed in the outer region, but the Friedel's salt contents barely changed. These results indicated that when there were sufficient SO_4^{2-} and Cl^- ions in the seawater curing environment, SO_4^{2-} ion would preferentially combine with Ca^{2+} and Al^{3+} ions, compared with Cl^- ion, forming AFt. With respect to the amorphous hydration products, the structure of C-S-H gel was seriously affected by using seawater as the curing water, i.e., the pore volume of C-S-H in the outer region, as shown in Fig. 3, was largely increased compared to the inner region.

4.2 Relation between the physical properties and the chemical changes

Firstly, the impedance modulus changed with the change of ion transport properties. The active ions in the seawater effectively contributed to the transport of electric current, and thus the impedance modulus of the SS sample was lower at 1 day than that of the DD sample. However, the MH crystals deposited on the concrete surface (Fig. 6) would influence the current transport, and thus the SS sample had a higher impedance modulus at 7 and 28 days. Also, the formed MH crystals increasingly grew and significantly blocked the surface, leading to the further increase of the impedance modulus of the SS sample at 28 days, compared to the results at 7 days.

Secondly, the inferior later-age strength of SS samples compared to DD samples was related to the chemical changes. The present study revealed that on one hand, the change of crystalline hydration products negatively affected the mechanical strength of the SS sample. Firstly, more ettringite crystals were formed at the later age in the outer region and lowered the compressive

strength of the SS sample. In Table 1, the AFt contents formed in the inner and middle regions of SS samples were similar, but that in the outer region of the SS sample dramatically increased to about three times (7 days) and four times (28 days) the AFt content in the other regions. In this work, curing in seawater enabled AFt to quickly form in the outer region of the SS sample. The high supersaturation of the pore solution with respect to AFt may explain the expansion and cracking [45]. In this work, the unlimited sulfate supply in the seawater caused AFt to form in the outside region of the SS sample, and a high total volume of AFt formed generated potential crystallization pressure [45], and subsequently affected the mechanical strength. Since the SS sample had a dense pore structure at a later age, the mechanical strength of the SS sample was negatively affected when more AFt crystals formed, grew, and induced expansion crack at the later stage. Secondly, the conversion between AFt crystal and Friedel's salt in the outer region, as shown in Table 1, might also be unfavorable to mechanical strength. Lastly, the formation of $Mg(OH)_2$ and the dissolution of $Ca(OH)_2$ further decreased the mechanical strength of the SS sample. According to the results in section 3.3, (i) the dissolution of CH would result in the increase of porosity in the outer section, and (ii) fresh MH was only formed on the surface or in the solution, and had no contribution to the mechanical strength, both of which seriously affected the bonding ability of SS sample. On the other hand, the change in the structure of the C-S-H gel might further decrease the compressive strength of the SS sample. As shown in Table 2, the mean molecular chain length and polymerization degree of C-S-H gel were decreased, which would further result in inferior bonding ability. In addition, amounts of nano-pores or gel pores of the SS sample significantly increased compared with the DD sample (Fig. 3), especially in the outer region, which would further affect the mechanical properties of the specimens.

Thermodynamic modeling was used to predict the long-term hydration product compositions of the seawater mixing and curing OPC pastes, as shown in Fig. 9. Furthermore, this GEMS model can predict the relative amounts of hydration products located in different regions of the specimen, i.e., the left-hand side of the figure represents the hydration product compositions on the surface or dissolved in the pore solution of the specimen. Progressively the right-hand side of the figure represents the product evolution at different depths of the specimen. The long-term phase compositions and contents in the outer region of the SS sample would further evolve compared with that at 28 days (Fig. 1 and Table 1), at which time a large amount of MH was formed, CH was absent, AFt content would further increase, and Friedel's salt was decomposed, which might further degrade the compressive strength of SS sample. On the surface of the SS sample which was exposed to higher levels of seawater, AFt and C-S-H phase would disappear; and correspondingly, a large amount of M-S-H, MH, and OH-hydrotalcite would be formed. The latter phases would be dissolved in the seawater environment, further reducing the strength of the cement paste.

De Weerdt et al. [17] also reported similar thermodynamic modeling, which mainly focuses on the seawater corrosion of cement paste mixed with freshwater. However, when seawater was used for both of mixing water and curing water, the product compositions changed, i.e., Friedel's salt would be present continuously in the inner region of the sample. Additionally, the experimental results in this work could further confirm the accuracy of the thermodynamic modeling, i.e., by comparing the other regions with the outer region of the 28 days SS sample, (i) the CH content

decreased and MH was formed (Table 1 and Figs. 5 and 6), and (ii) Friedel's salt content decreased and AFt content increased (Table 1), which were consistent with the results shown in Fig. 9.

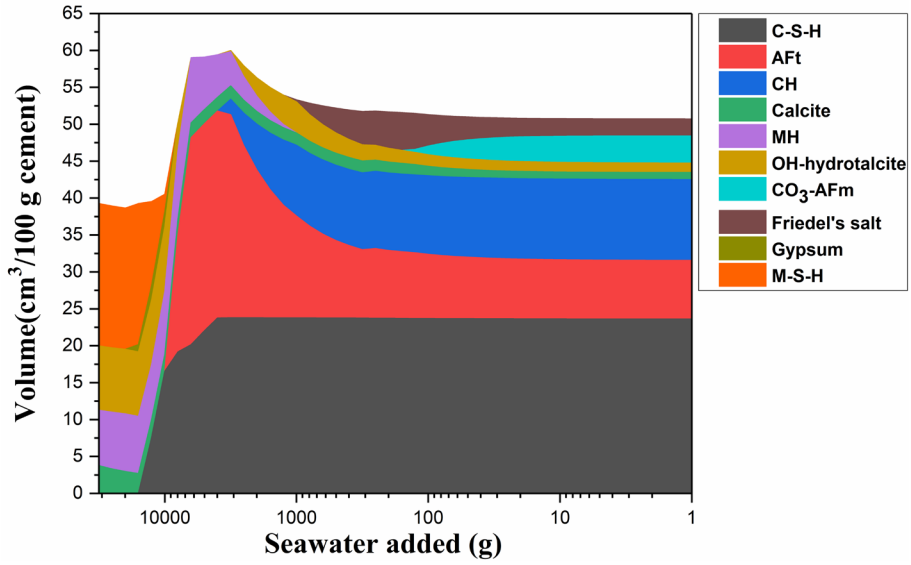

Fig. 9 Predicted volume of hydration products formed in the seawater mixed OPC paste exposed to seawater.

4. Conclusions

In this work, seawater was used for directly mixing and curing OPC pastes. The chemical changes were analyzed, and the relation between physical properties and chemical changes was further investigated. The main conclusions are summarized as follows.

1. The evolution of crystalline hydration products in different regions of the seawater mixing and curing OPC pastes was quantified. The AFt content in the outer region of the seawater mixed and cured (SS) specimen dramatically increased starting from 7 days, compared to the inner and middle regions. However, the Friedel's salt contents in the outer regions decreased slightly. A large amount of CH crystal in the outer region was dissolved while ($Mg(OH)_2$ (MH) crystal was formed on the surface with a lamellar morphology, exhibiting a much larger particle size compared to that formed in the solution.

2. The change in C-S-H structure was characterized. The polymerization degree and mean molecular chain length of C-S-H gel obviously decreased. Cl^- and Na^+ ions in seawater were incorporated into the interlayer of C-S-H gel, and the incorporation of Na^+ would form more silica dimers with a shorter silica chain. Moreover, the total pore volume of the SS sample increased by 22% in the inner region and 36% in the outer region compared with the DI water mixed and cured (DD) sample.

3. The change of physical properties was related to the chemical evolution. Firstly, the use of seawater increased the ion transport, but the MH crystals blocked the surface of the SS sample, largely reducing the ion transport. Secondly, the use of both mixing seawater and curing seawater influenced the strength development of the SS sample starting from 7 days. A higher amount of AFt crystal was formed in the outer region at a later age, which would generate potential expansion cracks since the samples had become hardened. The dissolution of CH would increase the porosity, and the formed MH had little contribution to the compressive strength. The change of C-S-H gel might also induce strength degradation. The C-S-H gel was formed with a shorter silica chain, which increased the total pore volume, especially in the outer region, and thus potentially decreased the cross-linking ability and compressive strength.

Acknowledgments

We wish to thank the financial support of the Research Grants Council Theme-Based Research Scheme (Project No. T22-502/18-R). We acknowledge the help of Dr. Kenneth and the support of the University Research Facility on Chemical and Environmental Analysis (UCEA) of PolyU.

References

[1] F. Zou, K. Shen, C. Hu, F. Wang, L. Yang, S. Hu, Effect of sodium sulfate and C-S-H Seeds on the reaction of fly ash with different amorphous alumina contents, ACS Sustainable Chem. Eng. 8 (3) (2019) 1659-1670.

[2] W. Song, J. Yi, H. Wu, X. He, Q. Song, J. Yin, Effect of carbon fiber on mechanical properties and dimensional stability of concrete incorporated with granulated-blast furnace slag, J. Clean. Prod. 238 (2019) 117819.

[3] J. Xiao, C. Qiang, A. Nanni, K. Zhang, Use of sea-sand and seawater in concrete construction:

Current status and future opportunities, Constr. Build. Mater. 155 (2017) 1101-1111.
[4] M. Guo, B. Hu, F. Xing, et al., Characterization of the mechanical properties of eco-friendly concrete made with untreated sea sand and seawater based on statistical analysis, Constr. Build. Mater. 234 (2020) 117339.
[5] T. Nishida, N. Otsuki, H. Ohara, et al. Some considerations for applicability of seawater as mixing water in concrete, J. Mater. Civ. Eng. 27 (7) (2015). B4014004-1-7.
[6] P. Li, W. Li, T. Yu, F. Qu, V.W.Y. Tam, Investigation on early-age hydration, mechanical properties and microstructure of seawater sea sand cement mortar, Constr. Build. Mater. 249 (2020) 118776.
[7] Y. Chen, C. Xia, Z. Shepard, et al., Self-Healing Coatings for Steel-Reinforced Concrete, ACS Sustainable Chem. Eng. 5 (5) (2017) 3955-3962.
[8] F. Wang, S. Lei, J. Ou, et al., Superhydrophobic calcium aluminate cement with super mechanical stability, Ind. Eng. Chem. Res. 58 (24) (2019) 10373-10382.
[9] Z. Wang, X. Zhao, G. Xian, et al., Long-term durability of basalt- and glass-fiber reinforced polymer (BFRP/GFRP) bars in seawater and sea sand concrete environment, Constr. Build. Mater. 139 (2017) 467-489.
[10] M. Bazli, Y. Li, X. Zhao, et al., Durability of seawater and sea sand concrete filled filament wound FRP tubes under seawater environments, Compos B Eng 202 (2020) 108409.
[11] J. Teng, Y. Xiang, T. Yu, Z. Fang, Development and mechanical behaviour of ultra-high-performance seawater sea-sand concrete, Adv. Struct. Eng. 22 (14) (2019) 3100-3120.
[12] S.K. Kaushik, S. Islam, Suitability of sea water for mixing structural concrete exposed to a marine environment, Cem. Concr. Compos. 17 (3) (1995) 177-185.
[13] A. Younis, U. Ebead, P. Suraneni, A. Nanni, Fresh and hardened properties of seawater-mixed concrete, Constr. Build. Mater. 190 (2018) 276-286.
[14] J. Wang, E. Liu, L. Li, Multiscale investigations on hydration mechanisms in seawater OPC paste, Constr. Build. Mater. 191 (2018) 891-903.
[15] R. Ragoug, O.O. Metalssi, F. Barberon, et al., Durability of cement pastes exposed to external sulfate attack and leaching: Physical and chemical aspects, Cem. Concr. Res. 116 (2019) 134-145.
[16] G. Li, A. Zhang, Z. Song, C. Shi, Y. Wang, J. Zhang, Study on the resistance to seawater corrosion of the cementitious systems containing ordinary Portland cement or/and calcium aluminate cement, Constr. Build. Mater. 157 (2017) 852-859.
[17] K. De Weerdt, B. Lothenbach, M.R. Geiker, Comparing chloride ingress from seawater and NaCl solution in Portland cement mortar, Cem. Concr. Res. 115 (2019) 80-89.
[18] X. Huang, S. Hu, F. Wang, L. Yang, M. Rao, Y. Tao, Enhanced sulfate resistance: the importance of iron in aluminate hydrates, ACS Sustainable Chem. Eng. 7 (7) (2019) 6792-6801.
[19] L. Montanari, P. Suraneni, M. Tsui-Chang, et al., Hydration, pore solution, and porosity of cementitious pastes made with seawater. J. Mater. Civ. Eng. 31(8) (2019) 04019154.
[20] J. Zhang, G.W. Scherer, Comparison of methods for arresting hydration of cement, Cem. Concr. Res. (10) (2011) 1024-1036.
[21] W. Hummel, U. Berner, E. Curti, F. Pearson, T. Thoenen, Nagra/PSI chemical thermodynamic data base 01/01, Radiochimica Acta, 90 (2002) 805-813
[22] B. Lothenbach, D.A. Kulik, T. Matschei, et al., Cemdata18: A chemical thermodynamic database for hydrated Portland cements and alkali-activated materials, Cem. Concr. Res. 115 (2019) 472-506.

[23] M. Santhanam, M. Cohen, J. Olek, Differentiating seawater and groundwater sulfate attack in Portland cement mortars, Cem. Concr. Res. 36 (12) (2006) 2132-2137.
[24] Z. Shi, Z. Shui, Q. Li, H. Geng, Combined effect of metakaolin and sea water on performance and microstructures of concrete, Constr. Build. Mater. 74 (2015) 57-64.
[25] K. De Weerdt, H. Justnes, M.R. Geiker, Changes in the phase assemblage of concrete exposed to sea water, Cem. Concr. Compos. 47 (2014) 53-63.
[26] J. Wang, B. Han, Z. Li, et al., Effect investigation of nanofillers on CSH gel structure with Si NMR, J. Mater. Civ. Eng. 31(2018) 04018352.
[27] D. Wang, Y. Fang, Y. Zhang, J. Chang, Changes in mineral composition, growth of calcite crystal, and promotion of physico-chemical properties induced by carbonation of β-C_2S, J. CO_2 Util. 34 (2019) 149-162.
[28] D. Da Silva Andrade, J.H. Da Silva Rêgo, P.C. Morais, et al., Investigation of C-S-H in ternary cement pastes containing nanosilica and highly-reactive supplementary cementitious materials (SCMs): Microstructure and strength, Constr. Build. Mater. 198 (2019) 445-455.
[29] Z. Jiang, Y. Xi, X. Gu, Q. Huang, W. Zhang, Modelling of water vapour sorption hysteresis of cement-based materials based on pore size distribution, Cem. Concr. Res. 115 (C) (2019) 8-19.
[30] Y. Dhandapani, M. Santhanam, Assessment of pore structure evolution in the limestone calcined clay cementitious system and its implications for performance, Cem. Concr. Compos. 84 (2017) 36-47.
[31] C. Qiao, P. Suraneni, T. Nathalene Wei Ying, A. Choudhary, J. Weiss, Chloride binding of cement pastes with fly ash exposed to $CaCl_2$ solutions at 5 and 23 °C, Cem. Concr. Compos. 97 (2019) 43-53.
[32] H. Hirao, K. Yamada, H. Takahashi, H. Zibara, Chloride binding of cement estimated by binding isotherms of hydrates, J. Adv. Concr. Technol. 3 (1) (2005) 77-84.
[33] M.V.A. Florea, H.J.H. Brouwers, Chloride binding related to hydration products, Cem. Concr. Res. 42 (2) (2012) 282-290.
[34] K. De Weerdt, A. Colombo, L. Coppola, H. Justnes, M.R. Geiker, Impact of the associated cation on chloride binding of Portland cement paste, Cem. Concr. Res. 68 (2015) 196-202.
[35] B. Lothenbach, A. Nonat, Calcium silicate hydrates: Solid and liquid phase composition, Cem. Concr. Res. 78 (2015) 57-70.
[36] I.G. Richardson, Model structures for C-(A)-S-H(I), Acta Crystallogr. B 70 (2014) 903-923
[37] D. Palin, H.M. Jonkers, V. Wiktor, Autogenous healing of sea-water exposed mortar: Quantification through a simple and rapid permeability test, Cem. Concr. Res. 84 (2016) 1-7.
[38] M. Abd El. Aziz, S. Abd El. Aleem, M. Heikal, H. El. Didamony, Hydration and durability of sulphate-resisting and slag cement blends in Caron's Lake water, Cem. Concr. Res. 35 (8) (2005) 1592-1600.
[39] D. Bonen, M. D. Cohen. Magnesium sulfate attack on portland cement paste-II. Chemical and mineralogical analyses, Cem. Concr. Res. 22 (4) (1992) 707-718
[40] Y. Wang, G. Kong, C. Che, Corrosion behavior of Zn-Al alloys in saturated $Ca(OH)_2$ solution, Corros. Sci. 112 (2016) 679-686.
[41] D. Buggio, M. Trueba, S.P. Trasatti, Corrosion of Mg alloy in the presence of ammonium ion. Evidence of hydride sub-products, Corros. Sci. 104 (2016) 173-186.
[42] M. Malbois, B. Nedjar, S. Lavaud, et al., On DEF expansion modelling in concrete structures under variable hydric conditions, Constr. Build. Mater. 207 (2019) 396-402.

[43] Y. Cai, D. Xuan, C.S. Poon, Effects of nano-SiO_2 and glass powder on mitigating alkali-silica reaction of cement glass mortars, Constr. Build. Mater. 201 (2019) 295-302.
[44] Y. Zhang, Y. Sun, H. Zheng, Y. Cai, W.L. Lam, C.S. Poon, Mechanism of strength evolution of seawater OPC pastes, Adv. Struct. Eng. 24 (6) (2021) 1256-1266.
[45] J. Bizzozero, C. Gosselin, K.L. Scrivener, Expansion mechanisms in calcium aluminate and sulfoaluminate systems with calcium sulfate, Cem. Concr. Res. 56 (2014) 190-202.